



Cite this: *RSC Adv.*, 2024, 14, 2354

# Dispersed MnO<sub>2</sub> nanoparticles/sugarcane bagasse-derived carbon composite as an anode material for lithium-ion batteries†

Krittaporn Pongpanyanate,<sup>a</sup> Supacharee Roddech,<sup>b</sup> <sup>\*ac</sup> Chanita Piyanirund,<sup>a</sup> Thanya Phraewphiphat<sup>d</sup> and Panitat Hasin<sup>bc</sup>

Bagasse-derived carbon electrodes were developed by doping with nitrogen functional groups and compositing with high-capacity MnO<sub>2</sub> nanoparticles (MnO<sub>2</sub>/NBGC). The bagasse-derived biochar was N-doped by refluxing in urea, followed by the deposition of MnO<sub>2</sub> nanoparticles onto its porous surface via the hydrothermal reduction of KMnO<sub>4</sub>. Different initial KMnO<sub>4</sub> loading concentrations (*i.e.* 5, 10, 40, and 100 mM) were applied to optimize the composite morphology and the corresponding electrochemical performance. Material characterization confirmed that the carbon composite has a mesoporous structure along with the dispersion of MnO<sub>2</sub> nano-particles on the N-containing carbon surface. It was found that the 5-MnO<sub>2</sub>/NBGC sample exhibited the highest electrochemical performance with a reversible capacity of 760 mA h g<sup>-1</sup> at a current density of 186 mA g<sup>-1</sup>. It delivered reversible capacities of 488 and 390 mA h g<sup>-1</sup> in cycle tests at 372 and 744 mA g<sup>-1</sup>, respectively, for 150 cycles and presented good reversibility with nearly 100% coulombic efficiency. In addition, it could exert high capacities up to 388 and 301 mA h g<sup>-1</sup> even under high current densities of 1860 and 3720 mA g<sup>-1</sup>, respectively. Moreover, most of the prepared composite products showed high rate capability with great reversibility up to more than 90% after testing at a high current density of 3720 mA g<sup>-1</sup>. The great electrochemical performance of the MnO<sub>2</sub>/NBGC nanocomposite electrode can be attributed to the synergistic impact of the hierarchical architecture of the MnO<sub>2</sub> nanocrystals deposited on porous carbon and the capacitive effect of the N-containing defects within the carbon material. The nanostructure of the MnO<sub>2</sub> particles deposited on porous carbon limits its large volume change during cycling and promotes good adhesion of MnO<sub>2</sub> nanoparticles with the substrate. Meanwhile, the capacitive effect of the exposed N-functional groups enables fast ionic conduction and reduces interfacial resistance at the electrode interface.

Received 14th June 2023  
Accepted 5th December 2023

DOI: 10.1039/d3ra04008a

rsc.li/rsc-advances

## Introduction

Currently, climate change, which is mainly caused by extensive carbon dioxide emissions from fossil fuel combustion, drives the demand for sustainable electrical energy generators and storage devices. Lithium-ion batteries (LIBs) have drawn much attention as effective energy storage and conversion devices for various electrical equipment ranging from small portable

devices and electricity-driven automobiles to electrical power plants owing to their high energy density, excellent cyclic stability, long lifetime, and low self-discharge features.<sup>1</sup> The anode material is considered as one of the key components that determine the performance of LIBs. Generally, most commercial LIBs use graphite as the active anode material because of its feasibility for mass production. However, the production cost of high-quality graphite is quite high; it requires a long reaction process and consumes a high amount of fossil fuel-based energy. Moreover, its theoretical capacity is only about 370 mA h g<sup>-1</sup> due to the limitation of the stoichiometric intercalation of lithium ions within the nominal graphitic layer.<sup>2</sup> In the past decades, hard carbon (HC) has emerged as an alternative carbonaceous anode material for LIBs to enhance the ionic storage capacity of typical crystalline graphite. This non-graphitic carbon is derived from small domains of graphene-like stacking layers (with dilated *d*-spacing) and embedded microporous regions (a “house of cards” structure).<sup>3</sup> This unique microstructure allows both ionic intercalation between

<sup>a</sup>Department of Chemical Engineering, Faculty of Engineering, Kasetsart University, Thailand

<sup>b</sup>Department of Chemistry and Center of Excellence for Innovation in Chemistry (PERCH-CIC), Ministry of Higher Education, Science, Research and Innovation, Faculty of Science, Kasetsart University, Thailand

<sup>c</sup>Kasetsart University Research and Development Institute, Kasetsart University, Thailand. E-mail: fengsrro@ku.ac.th

<sup>d</sup>National Energy Technology Center (ENTEC), 114 Thailand Science Park, Phaholyothin Road, Klong 1, Klongluang, Pathumthani, 12120, Thailand

† Electronic supplementary information (ESI) available. See DOI: <https://doi.org/10.1039/d3ra04008a>


the carbon layers and ionic adsorption on the surface defect sites, as well as ionic filling of the micropores.<sup>4</sup> HC is usually derived from the pyrolysis of biomass and polymeric carbon precursors, such as pitch, phenolic and epoxy resins. The resulting electrochemical ionic storage capability is generally influenced by the carbon precursor type, material morphology, carbonization temperature, and heteroatom doping.<sup>5–7</sup>

Recently, the sustainable concept of converting agricultural waste into porous carbon electrode materials is rapidly developing.<sup>8,9</sup> One of the promising biomass-based carbon precursors is sugarcane bagasse, which naturally has a high density of xylem and phloem that can facilitate the formation of porous carbon materials with abundant transport channels.<sup>3,10</sup> So far, research on the development of sugarcane-bagasse-derived carbon materials as potential anodes for LIBs has mostly been devoted to optimizing the preparation approach or employing elaborate methods to formulate highly porous structures.<sup>10–12</sup> Many studies have focused on doping with heteroatoms, such as nitrogen, sulphur, and phosphorus-containing functional groups, to promote charge storage capability and ionic conduction, which ultimately increase the cycling stability of the carbon electrode materials. The capacitive effect arising from their electron-donating characteristic leads to a reduction in interfacial resistance between the electrode and the aqueous electrolyte.<sup>13,14</sup>

Meanwhile, transition metal oxides (MO) have also emerged as attractive electrode materials for LIBs. In particular, manganese oxide, as  $\text{MnO}_2$ , has been regarded as a promising electrode material owing to its high theoretical capacity of  $1230 \text{ mA h g}^{-1}$ , abundance, low cost, and environment-friendly nature. Moreover, it is the main composing material in primary alkaline batteries and can be recycled from disposed batteries. However, as an anode material,  $\text{MnO}_2$  typically shows fast capacity fading due to the large volume change during the lithium insertion-desertion process. One of the potential methods to improve the mechanical stability of  $\text{MnO}_2$ -based electrodes is to deposit it onto a supporting material or form a porous structure.<sup>15,16</sup>

Therefore, this research was aimed at developing a modified bagasse-derived carbon anode material for LIBs. The electrochemical performance of the bagasse-based carbon material was enhanced by doping it with nitrogen functional groups using urea as the precursor, followed by the deposition of different amounts of  $\text{MnO}_2$  nanoparticles on the carbon substrate *via* the reduction of  $\text{KMnO}_4$  at various initial concentrations. The doped N-containing functional groups in conjunction with the  $\text{MnO}_2$  nanocomposite are expected to promote ionic conduction and lithium storage capability. Meanwhile, the  $\text{MnO}_2$  nanoparticles deposited onto the bagasse-based porous carbon substrate would improve the cycling stability of the  $\text{MnO}_2$  compound from a large volume expansion during the conversion process. The carbon composite products prepared with different  $\text{KMnO}_4$  loadings were analyzed to investigate the impact of  $\text{KMnO}_4$  loading on composite morphology and corresponding electrochemical performance.

## Experimental details

Sodium hydroxide ( $\text{NaOH}$ ), calcium chloride ( $\text{CaCl}_2$ ) and urea ( $\text{CH}_4\text{N}_2\text{O}$ ) were obtained from Kemaus. Hydrochloric acid ( $\text{HCl}$ , 37%) and potassium permanganate ( $\text{KMnO}_4$ ) were obtained from QRc. All chemicals were used as received without purification.

### Preparation of N-containing sugarcane-bagasse-derived carbon material (NBGC)

7.5 g of sugarcane bagasse was soaked in 10% w/v  $\text{NaOH}$  for 30 minutes, washed with DI water until a pH of around 6.5–7 was reached and dried at  $80^\circ\text{C}$  overnight. Dried sugarcane bagasse was then dispersed in 0.5 M sulfuric acid inside a Teflon-lined autoclave and heated at  $180^\circ\text{C}$  for 24 hours. Subsequently, the solid residue was filtered, washed with DI water, and dried at  $80^\circ\text{C}$  overnight to obtain the biochar product. Later, the obtained biochar was mixed with  $\text{CaCl}_2$  and urea at a carbon material :  $\text{CaCl}_2$  : urea weight ratio of 1 : 2 : 2 in 50 mL DI water and refluxed at  $80^\circ\text{C}$  for 4 hours. After cooling to room temperature, the solid product was filtered and pyrolyzed at  $800^\circ\text{C}$  for 2 hours under a nitrogen atmosphere at a heating rate of  $5^\circ\text{C min}^{-1}$ . After the pyrolysis process, the N-doped carbon material was soaked in 2 M  $\text{HCl}$  under stirring for 1 hour and washed with DI water until the pH reached around 6–7. After drying in a vacuum oven at  $105^\circ\text{C}$  for 12 hours, the N-doped sugarcane-bagasse-derived carbon material (NBGC) was achieved as a fine black powder.

### Synthesis of $\text{MnO}_2$ nanoparticle-dispersed N-doped sugarcane-bagasse-derived porous carbon composite ( $\text{MnO}_2/\text{NBGC}$ )

0.3 g of the obtained NBGC was dispersed in 80 mL of aqueous potassium permanganate ( $\text{KMnO}_4$ ) solutions with different initial concentrations of 5, 10, 40 and 100 mM, respectively. Each mixture was well mixed by sonication for 1 hour. After transferring to a Teflon-lined autoclave, the mixture was heated up at  $140^\circ\text{C}$  for 2 hours and then cooled to room temperature. The solid product was filtered, washed with DI water, and dried at  $80^\circ\text{C}$  overnight. The achieved  $\text{MnO}_2/\text{NBGC}$  carbon composite products were named based on the different initial  $\text{KMnO}_4$  concentrations (*i.e.*, 5, 10, 40, and 100 mM) as 5- $\text{MnO}_2/\text{NBGC}$ , 10- $\text{MnO}_2/\text{NBGC}$ , 40- $\text{MnO}_2/\text{NBGC}$ , and 100- $\text{MnO}_2/\text{NBGC}$ , respectively. As a reference, pure  $\text{MnO}_2$  was solely synthesized by employing the same procedure without NBGC addition. In detail, 180 mL of a 50 mM  $\text{KMnO}_4$  solution was sonicated for an hour and then transferred to the Teflon-lined autoclave. The solution was heated at  $140^\circ\text{C}$  for 24 hours. The obtained solid was filtered, washed, and dried at  $80^\circ\text{C}$  overnight.

### Material characterization

The crystallographic information of the products was obtained using X-ray diffraction (XRD, Bruker D8 Advance) with  $\text{Cu-K}\alpha$  radiation  $\lambda = 1.54060 \text{ \AA}$  and  $2\theta = 10^\circ$  to  $80^\circ$ . The morphologies of the carbon composites with porous  $\text{MnO}_2$  coatings were



characterized by scanning electron microscopy (SEM) and transmission electron microscopy (TEM) with a high tension of 120 kV (HITACHI-HT7700). The surface elemental analysis of the samples was carried out using energy-dispersive X-ray spectroscopy (FEI, QUANTA 450), and the bulk C, H, and N contents were analyzed by an Elemental Analyzer (LECO, CHN628 Series). X-ray photoelectron spectroscopy (XPS) was used to analyse the surface functional groups on the carbon composite products.  $N_2$  adsorption-desorption measurement (Quantachrome ASIC-2) was employed to obtain the specific surface area based on the Brunauer-Emmett-Teller theory (BET).

### Electrochemical performance evaluation

The electrochemical performance of the  $MnO_2$ /NBGC carbon composite products was assessed by assembling coin cells (CR2032). The anode material slurry was composed of 80 wt% of the prepared  $MnO_2$ /NBGC carbon composite, 10 wt% of Super P conductive carbon, and 10 wt% of polyvinylidene fluoride (PVDF) in *N*-methylpyrrolidone, which was used as a binder. After vigorous mixing for 3 hours, the mixture was cast on a copper foil, followed by drying overnight at 70 °C in a vacuum oven. Then, the cast anode was cut into circle-shaped specimens of radius 14 mm, which approximately contained 2 mg of the dried material. Subsequently, the prepared anode electrode was assembled with a lithium metal counter electrode, Celgard2320 (PP/PE/PP) separator, and 1 M  $LiPF_6$  in the electrolyte mixture of 1 : 1 : 1 v/v EC : EMC : DMC. The testing cells were charged and discharged between 0.01 and 3.0 V relative to  $Li/Li^+$  at various current densities by using an electrochemical charge-discharge tester (Gelon company Neware BTS-4000). Cyclic voltammetry (CV) measurements were performed in the potential window of  $-0.1$  to 3 V relative to  $Li/Li^+$  at a scan rate of  $1-2.2\text{ mV s}^{-1}$  to investigate the electrode reaction mechanism

by using a potentiostat/galvanostat (Autolab PGSTAT101). Finally, electrochemical impedance spectroscopy (EIS) (Versa-STAT3 Potentiostat Galvanostat, Princeton Applied Research, USA) was used to measure the electrochemical impedance of the electrode in the frequency range of 0.1–100 000 Hz and at the voltage of 10 mV.

## Results and discussion

The morphologies of the bagasse-derived carbon material products and hydrothermally synthesized  $MnO_2$  nanoparticles were observed by using FESEM (Fig. 1a–g) and TEM (Fig. 2a–f). The bagasse-derived carbon materials (BGC) showed honeycomb-like porous structures that depict their natural xylem and phloem transporting channels with macropores of diameter about 5–8  $\mu\text{m}$  and relatively thick walls. After refluxing bagasse with urea to insert N-containing functional defects, the obtained N-doped bagasse-based carbon (NBGC) material exhibited a slightly smoother surface compared to pristine bagasse. The collapse of some connecting walls within the parent bagasse carbon during the reflux process resulted in merged pores, leading to a larger pore size in the N-containing carbon compound, as listed in Table 1. Composites with dispersed manganese dioxide ( $MnO_2$ ) nanoparticles at various loading contents on N-containing bagasse-derived porous carbon ( $MnO_2$ /NBGCs) were prepared by using different concentrations of the potassium permanganate ( $KMnO_4$ ) precursor (e.g. 5, 10, 40, and 100 mM). Likewise, the  $MnO_2$ /NBGC composites obtained with different  $KMnO_4$  loading concentrations retained the honeycomb-like porous structure of the parent bagasse-based carbon substrate. The porous structure of the  $MnO_2$ /NBGC composite can accommodate the large volume expansion of the  $MnO_2$  compound during the  $Li^+$  insertion/desertion process. It was found that the increase in

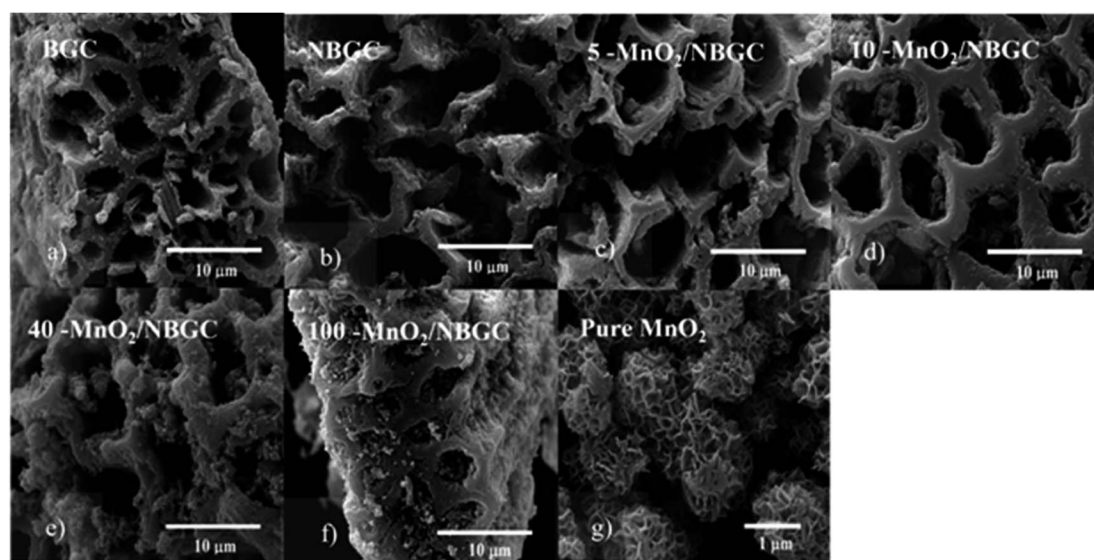


Fig. 1 SEM images of the prepared bagasse-based carbon materials: (a) bagasse-derived carbon material (BGC), (b) N-doped bagasse-derived carbon material (NBGC), and  $MnO_2$ /N-doped bagasse-derived carbon composites with different loading concentrations ( $MnO_2$ /NBGC): (c) 5- $MnO_2$ /NBGC, (d) 10- $MnO_2$ /NBGC, (e) 40- $MnO_2$ /NBGC, (f) 100- $MnO_2$ /NBGC, and (g) hydrothermally synthesized pure  $MnO_2$ .





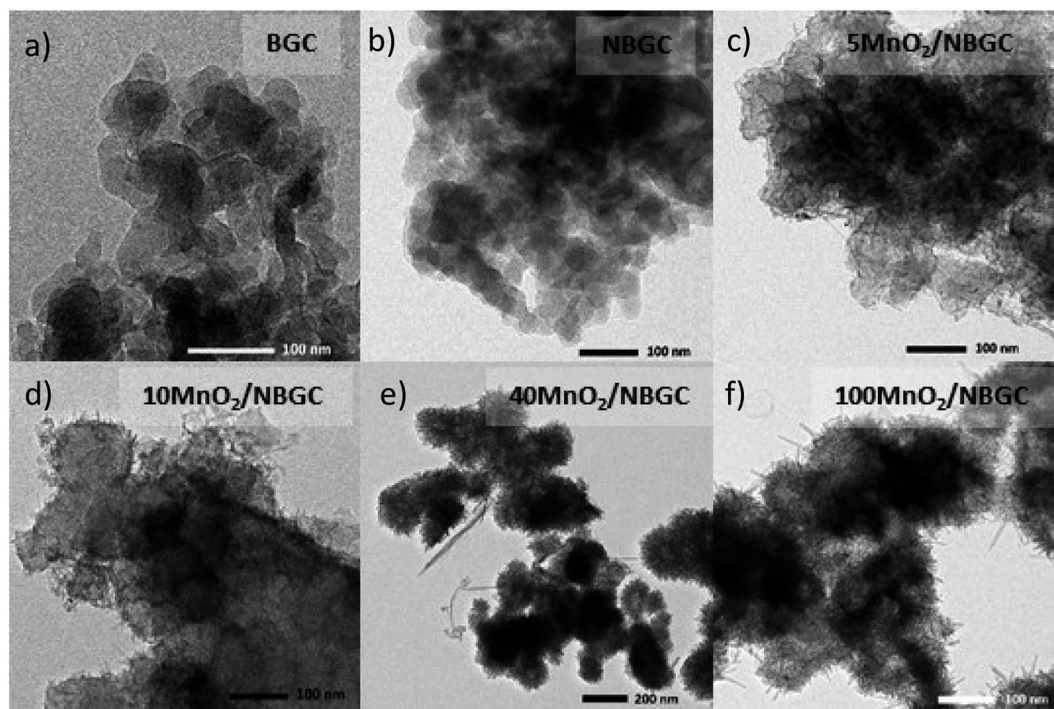


Fig. 2 TEM images of the prepared bagasse-based carbon material: (a) bagasse-derived carbon material (BGC), (b) N-doped bagasse-derived carbon material (NBGC),  $\text{MnO}_2$ /N-doped bagasse-derived carbon composite at different loading concentrations ( $\text{MnO}_2$ /NBGC): (c) 5- $\text{MnO}_2$ /NBGC, (d) 10- $\text{MnO}_2$ /NBGC, (e) 40- $\text{MnO}_2$ /NBGC, and (f) 100- $\text{MnO}_2$ /NBGC.

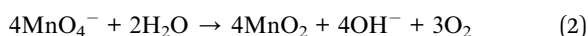
the applied  $\text{KMnO}_4$  precursor led to more agglomeration of the  $\text{MnO}_2$  nanoparticles, ultimately resulting in thicker  $\text{MnO}_2$  coatings on the porous surface. This thick coating layer can block the pore channels and cause a reduction in the specific surface area of the electrode material. As the reference, pure  $\text{MnO}_2$  nanoparticles were also synthesized by the hydrothermal reaction in the absence of the bagasse-based carbon substrate. As seen in Fig. 1g, without the carbon substrate, the synthesized  $\text{MnO}_2$  nanocrystals exhibited radial growth and became spherical coral-like particles with an average diameter of around 1  $\mu\text{m}$ . Similarly, the TEM images shown in Fig. 2c–f also reveal a coating layer of  $\text{MnO}_2$  on the bagasse-derived carbon surface. Meanwhile, only clusters of carbon material without any coating layer or spike-like coating were observed in the cases of BGC and NBGC. At a low concentration of  $\text{KMnO}_4$ , as in samples 5- $\text{MnO}_2$ /NBGC and 10- $\text{MnO}_2$ /NBGC, only a thin  $\text{MnO}_2$  coating layer was formed on the surface of porous carbon. At higher

loading concentrations of the  $\text{KMnO}_4$  precursor, as in the samples 40- $\text{MnO}_2$ /NBGC and 100- $\text{MnO}_2$ /NBGC, the rapid growth of the  $\text{MnO}_2$  clusters led to thicker coating layers on the carbon surface, forming numerous tiny nanoflakes. This obtained caterpillar-like nanostructure was similar to the porous  $\text{MnO}_2$  nanocomposite reported by Xia *et al.*<sup>16</sup> who synthesized  $\text{MnO}_2$  coating layers on carbon nanotubes *via* a similar procedure. These  $\text{MnO}_2$  nanoflakes were interconnected and uniformly distributed on the carbon surface. By controlling the  $\text{KMnO}_4$  loading concentration, the thickness of the  $\text{MnO}_2$  layer could be practically varied. The mechanism of  $\text{MnO}_2$  nanocrystal growth on the carbon material can be explained by the reduction reaction of  $\text{KMnO}_4$ .<sup>17</sup> Briefly, the N-doped carbon material (NBGC) was initially dispersed well in a  $\text{KMnO}_4$  solution, which was subjected to a hydrothermal reaction to produce the final carbon composite product. During mixing within the  $\text{KMnO}_4$  solution at room temperature,

Table 1 Surface morphology and contents of the crystalline bagasse-derived carbon composites with different  $\text{MnO}_2$  loading contents, as analyzed by Raman spectroscopy

Carbon composite	Specific surface area ( $\text{m}^2 \text{g}^{-1}$ )	Pore volume ( $\text{cm}^3 \text{g}^{-1}$ )	Avg. pore size (nm)	$I_d/I_g$
BGC	271.80	0.34	5.01	1.296
NBGC	210.63	0.29	5.59	1.251
5- $\text{MnO}_2$ /NBGC	183.11	0.23	4.97	1.233
10- $\text{MnO}_2$ /NBGC	178.93	0.23	5.82	1.187
40- $\text{MnO}_2$ /NBGC	144.51	0.17	4.76	1.231
100- $\text{MnO}_2$ /NBGC	105.61	0.11	4.01	1.245

nanocrystalline  $\text{MnO}_2$  seeds are generated on the surface of the porous carbon substrate *via* a slow redox process, according to eqn (1).<sup>16,18</sup> Once the solution further undergoes the hydrothermal reaction, the  $\text{MnO}_2$  nanoparticles grow from the pre-formed nanocrystalline seeds due to the decomposition of  $\text{KMnO}_4$  in water, according to eqn (2).<sup>16</sup> The flaky morphology is formed due to the preferred growth of the layered birnessite-type  $\text{MnO}_2$  along the *ab* plane.<sup>19</sup> Here, the layer of nanostructured  $\text{MnO}_2$  particles coated the surfaces of the porous carbon substrate uniformly to form nanocomposite products.



Surface elemental analysis using Energy-Dispersive Spectroscopy (EDS) and the C, H and N content analysis of the bagasse-derived carbon material and the  $\text{MnO}_2$ -doped carbon composite products with different degrees of doping are summarized in Table S1.† Based on surface EDS mapping, as a reference, the bagasse precursor was subjected to the hydrothermal reaction and carbonized at 800 °C but refluxed without urea addition. It transformed into a carbon material (BGC) that contained a high C content of about 92 wt%. However, oxygen-containing functional groups, such as oxy, hydroxyl, and carbonyl groups, which are typically found for bio-based carbon, were retained. In the NBGC compound, refluxing in the urea solution resulted in a nitrogen functional group content of approximately 5 wt%. Subsequently, dispersing NBGC in  $\text{KMnO}_4$  under a hydrothermal condition could deposit manganese oxide onto the carbon substrate, as indicated by the emergence of Mn content in the composite products. Increasing the loading concentration of the  $\text{KMnO}_4$  precursor caused the generation of more manganese oxide, as greater Mn wt% was observed. This was also confirmed by the results from the elemental analyzer, which demonstrated that C and N decreased as they were consumed during the formation of  $\text{MnO}_2$ . However, the differences in the amounts of C and N determined from EDS mapping and the elemental analyzer are attributed to the different collecting techniques. For instance, EDS generally maps the elements only on the surface and over some selected areas, whereas the C H N elemental analyzer provides bulk elemental analysis. The lower amount of C and N observed in the bulk analysis may result from the normalization of these elements with O and Mn from  $\text{MnO}_2$  and other related O-containing organic functional groups. Results from both techniques agree well with the observed SEM and TEM images, which revealed a thicker coating layer on the porous substrate for samples with higher  $\text{KMnO}_4$  loading contents. Notably, the N-containing defects are expected to support ionic conductivity and promote lithium-ion capacity. On the one hand,  $\text{MnO}_2$  accommodates high  $\text{Li}^+$  storage capability because of its high theoretical capacity. However, the formation of a thick  $\text{MnO}_2$  coating may not only block the exposed nitrogen functional groups and retard ionic transport but also readily inhibit the growth of its good crystalline structure.

Nitrogen adsorption/desorption analysis was conducted to investigate the pore morphology of BGC, NBGC, and the  $\text{MnO}_2$ /NBGC carbon composites. The sorption isotherms illustrated in Fig. S1† present type IV isotherms in the medium to high relative pressure range of about 0.5–1.0  $P/P_0$ , indicating mesoporous material characteristics. H3-type hysteresis loops at high pressures and nearly parallel adsorption and desorption branches at relative pressures between 0.05 and 0.5 were observed for all samples, revealing the presence of slit-shaped pores that enable the aggregation of plate-like particles. As summarized in Table 1, pristine bagasse-based porous carbon (BGC) showed a Brunauer–Emmett–Teller (BET) specific surface area of approximately  $271.80 \text{ m}^2 \text{ g}^{-1}$  with a specific pore volume of  $0.34 \text{ cm}^3 \text{ g}^{-1}$  and a pore size of 5.01 nm. Doping with N-containing compounds resulted in a reduction in the BET specific surface area to  $210.63 \text{ m}^2 \text{ g}^{-1}$  with a larger average pore size and a smaller specific pore volume. This is consistent with its corresponding SEM image (Fig. 1b), which reveals merged pores formed due to the collapse of the connecting walls within BGC. Further loading  $\text{MnO}_2$  on the obtained N-doped carbon tended to decrease the BET specific surface area of the carbon composite product. Increasing the  $\text{MnO}_2$  loading concentration led to smaller pore volumes and average pore sizes, which can be explained by the formation of thicker  $\text{MnO}_2$  coating layers that clog the pores of the bagasse-based parent carbon substrate. On the one hand, high content of  $\text{MnO}_2$  can promote electrode capacity because of its high theoretical capacity of  $1230 \text{ mA h g}^{-1}$ . However, coating a very thick  $\text{MnO}_2$  layer can cause a reduction in the active specific surface area and weak adhesion of the  $\text{MnO}_2$  layers on the porous carbon substrate, as well as shield the capacitive effect of the doped N-containing defects within the carbon material.

The X-ray diffraction patterns of BGC, NBGC, the carbon composite of porous NBGC with dispersed  $\text{MnO}_2$  particles at various loading concentrations ( $\text{MnO}_2$ /NBGC), and pure manganese dioxide ( $\text{MnO}_2$ ) are shown in Fig. 3. Bagasse-derived carbon (BGC) and its corresponding N-doped compound (NBGC) exhibited broad diffraction peaks at  $2\theta$  of approximately  $17^\circ$ ,  $32^\circ$  and  $44^\circ$ , indicating the characteristic (002) and (100) planes of the amorphous carbon structure with a low graphitization fraction.<sup>20</sup> Pure  $\text{MnO}_2$  synthesized from the hydrothermal reaction had XRD diffraction peaks at  $2\theta$  of  $12.8$ ,  $18.1$ ,  $28.9$ ,  $37.5$ ,  $42$ ,  $49.9$ ,  $60.3$  and  $65.4^\circ$ , representing the (110), (200), (310), (211), (301), (411), (600) and (002) planes of hollandite-type  $\alpha$ - $\text{MnO}_2$ , respectively (JCPDS 44-0141).<sup>21–23</sup> Compared to BGC and NBGC, the  $\text{MnO}_2$ /NBGC composite products at all  $\text{MnO}_2$  loading concentrations showed common XRD peaks at  $2\theta$  of approximately  $38^\circ$  and  $67^\circ$ , consistent with the main characteristic crystalline planes of  $\alpha$ - $\text{MnO}_2$ . All the diffraction peaks obtained from the deposited  $\text{MnO}_2$  nanoparticles were quite weak and broad, denoting their nanocrystalline nature. Interestingly, in the XRD patterns of all the  $\text{MnO}_2$ /NBGC carbon composite samples, the XRD peak at  $2\theta = 32^\circ$ , which represents the amorphous structure of the bagasse-derived parent carbon, was shifted to a lower diffraction angle of around  $2\theta = 25^\circ$ . This implies that the inserted  $\text{MnO}_2$  nanoparticles caused the expansion of the carbon plane structure such that the *d*-spacing



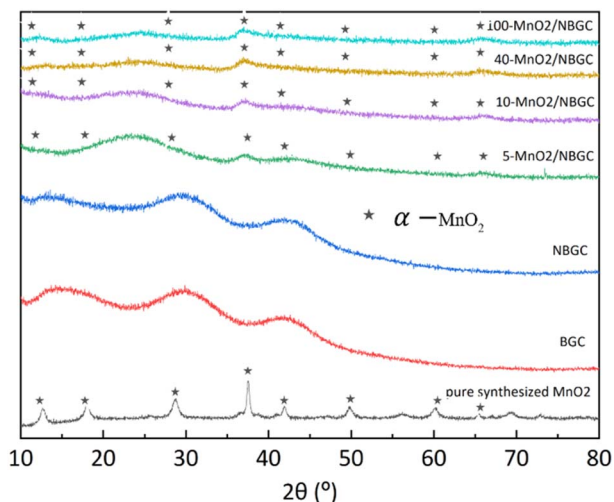


Fig. 3 The XRD spectra of BGC, NBGC, 5-MnO<sub>2</sub>/NBGC, 10-MnO<sub>2</sub>/NBGC, 40-MnO<sub>2</sub>/NBGC, 100-MnO<sub>2</sub>/NBGC, and pure MnO<sub>2</sub>.

of the carbon plane increased from about 1.5 Å to 1.9 Å, as calculated based on Bragg's law. This wider *d*-spacing can ultimately facilitate better accessibility of Li<sup>+</sup> or larger ions, such as Na<sup>+</sup> and K<sup>+</sup>. As the concentration of MnO<sub>2</sub> doping increased, the diffraction peaks from MnO<sub>2</sub> became stronger, whereas the diffraction peaks from the carbon parent became almost invisible. This indicates the growth of thicker MnO<sub>2</sub> layers covering the porous carbon substrate.

To further confirm the XRD results, the oxidation state and the composition of manganese oxide in the MnO<sub>2</sub>/NBGC nanocomposite products, as well as those of the bagasse-derived carbon material, were examined by X-ray photoelectron spectroscopy (XPS). As shown in Fig. S2a and b,<sup>†</sup> the wide survey XPS spectrum of BGC and NBGC comprised binding energy peaks at 285 and 533 eV, representing C 1s and O 1s. Meanwhile, as seen in Fig. S2c,<sup>†</sup> the XPS survey spectra of the

MnO<sub>2</sub>/NBGC composites with different MnO<sub>2</sub> loading concentrations showed a predominant signal of Mn 2p at the binding energy of around 642 eV in addition to the C 1s and O 1s peaks at 285 and 531 eV, respectively (Table S2<sup>†</sup>). Notably, signals of the N-containing defects in the carbon material were not clearly observed in all samples. This may be because of the very low nitrogen content (~5 wt% detected by EDS elemental mapping) in NBGC. According to the lower penetration depth of the XPS technique compared with that of the EDS technique, the MnO<sub>2</sub> coating layer may shield the signal of the N functional groups underneath in the case of MnO<sub>2</sub>/NBGC composites. The deconvoluted XPS spectra of the MnO<sub>2</sub>/NBGC composites are reported in Fig. 4. Fig. 4a shows the deconvoluted C 1s spectrum with four binding energy peaks at 284.9, 286.2, 287.3 and 288.7 eV, which represent graphitic carbon (C–C/C=C), C–O, C=O, and C=O–O, respectively.<sup>13,24</sup> The deconvoluted O 1s XPS spectrum, shown in Fig. 4b, indicates the bonds between manganese and lattice oxygen, as well as surface-adsorbed oxygen, including Mn–O–Mn, Mn–O–H and C–O/C=O, which correspond with the binding energy peaks at 530.2, 531.7 and 532.9 eV, respectively.<sup>15,24</sup> In Fig. 4c and d, the Mn 2p spectra exhibit well-defined valence states at binding energies approximately equal to 643.3 and 654.8 eV, which represent the Mn 2p<sub>3/2</sub> and Mn 2p<sub>1/2</sub> states, respectively. The difference between the two binding energy signals of Mn 2p was about 11.5 eV, which is the typical characteristic of Mn<sup>4+</sup> in MnO<sub>2</sub>.<sup>25</sup>

Raman spectroscopy was further employed to analyze the ordered structures of the MnO<sub>2</sub>/NBGC composite products (Fig. 5). The G band and D band of the carbon structure were observed around 1586–1604 cm<sup>−1</sup> and 1336–1354 cm<sup>−1</sup>, respectively. The weak bands at 630 cm<sup>−1</sup> were related to the symmetric stretching vibration of M–O in the MnO<sub>6</sub> groups.<sup>26</sup> The findings reveal that somehow doping carbon with N-containing functional groups and loading it with MnO<sub>2</sub> nanoparticles *via* thermal reduction of KMnO<sub>4</sub> result in a carbon structure with better crystallinity, as reflected by the lower values of *I*<sub>d</sub>/*I*<sub>g</sub> for NBGC and all MnO<sub>2</sub>/NBGC samples (Table 1). Perhaps, either refluxing under basic conditions or the

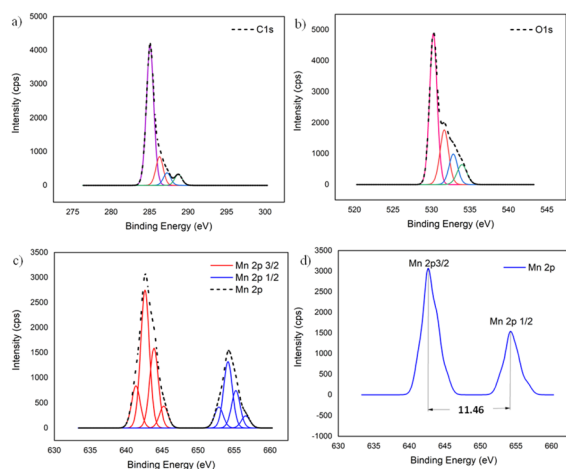


Fig. 4 The deconvoluted XPS spectra of MnO<sub>2</sub>/NBGC: (a) C 1s, (b) O 1s, and (c) Mn 2p; (d) binding energy difference between Mn 2p<sub>3/2</sub> and Mn 2p<sub>1/2</sub>.

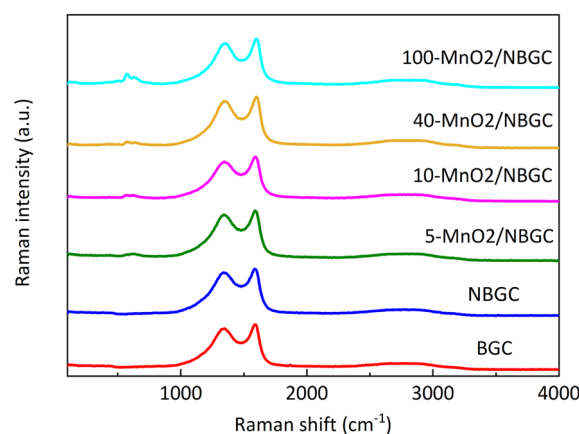


Fig. 5 The Raman spectra of BGC, NBGC and MnO<sub>2</sub>/NBGC with different MnO<sub>2</sub> loadings.





hydrothermal reduction of  $\text{KMnO}_4$  might catalyze the conversion of the bio-based amorphous carbon material into a carbon framework with better crystallinity. However, a continuous increase in  $\text{MnO}_2$  loading by enhancing  $\text{KMnO}_4$  concentration, such as the cases of 40- $\text{MnO}_2/\text{NBGC}$ , and 100- $\text{MnO}_2/\text{NBGC}$ , tended to drive the formation of more disordered carbon structures, as observed by their higher  $I_d/I_g$  ratios.

### Electrochemical performance evaluation

Cyclic voltammetry (CV) was used to investigate the lithium storage phenomena of the bagasse-based carbon materials (BGC and NBGC) and the  $\text{MnO}_2/\text{NBGC}$  composites when used as anode materials in the potential window of  $-0.01$ – $3.0$  V vs.  $\text{Li}/\text{Li}^+$  at a scan rate of  $2 \text{ mV s}^{-1}$ . As shown in Fig. 6a, the 1st CV scans of BGC and NBGC presented broad cathodic peaks at around  $0.3$  and  $0.4$  V, respectively, corresponding to the decomposition of the electrolyte into a solid coating interface (SEI). Meanwhile, the obvious anodic peak at approximately  $0.6$ – $0.7$  V corresponds to the de-intercalation of  $\text{Li}^+$  from the carbon structure. The sloped broad anodic peak in the range of  $0.7$ – $1.3$  V arises from the extraction of  $\text{Li}^+$  from the pores.<sup>27,28</sup> In general, the CV signal for the de-insertion of  $\text{Li}^+$  from the carbon material with a large surface area in the  $1000$ – $2000 \text{ m}^2 \text{ g}^{-1}$  range

will appear as a broad anodic peak.<sup>29–32</sup> The obvious anodic peaks of our carbon material that does not hold a very high specific surface area ( $\sim 271.80 \text{ m}^2 \text{ g}^{-1}$ ) may imply the greater influence of  $\text{Li}^+$  de-intercalation from the  $\text{MnO}_2$  compound over the de-insertion process typically found in high-surface-area biomass-based porous carbon materials. In the CV scans of the  $\text{MnO}_2/\text{NBGC}$  composites, the oxidation peaks observed at  $1.2$  V and  $2.3$  V represent the 2-step oxidation reaction of  $\text{Mn}^0$  to  $\text{Mn}^{2+}$  and  $\text{Mn}^{2+}$  to  $\text{Mn}^{4+}$ , respectively.<sup>33</sup> The more distinct anodic peaks of the composites with high  $\text{MnO}_2$  loading, such as 40- $\text{MnO}_2/\text{NBGC}$  and 100- $\text{MnO}_2/\text{NBGC}$ , may have resulted from the greater content of  $\text{MnO}_2$  in these composites. The cathodic peaks appearing at  $\sim 1$  V and  $0.4$  V correspond to the reduction of manganese oxide to metallic manganese ( $\text{Mn}^{4+}$  to  $\text{Mn}^0$ ) in conjunction with the formation of  $\text{Li}_2\text{O}$ <sup>34</sup> and SEI formation, respectively. The reaction mechanism can be described as shown in eqn (3) and (4); during discharge,  $\text{MnO}_2$  is reduced to Mn, and  $\text{Li}^+$  is converted to  $\text{Li}_2\text{O}$ . This lithiation typically leads to the formation of nanometer-scale metal clusters embedded in a  $\text{Li}_2\text{O}$  matrix accompanied by a large volume expansion. The formation of  $\text{Mn}/\text{Li}_2\text{O}$  leads to a theoretical capacity of  $1230 \text{ mA h g}^{-1}$  for  $\text{MnO}_2$ . During charging, Mn is oxidized to form  $\text{MnO}_2$ , while  $\text{Li}_2\text{O}$  is decomposed into  $\text{Li}^+$ .<sup>35–37</sup>

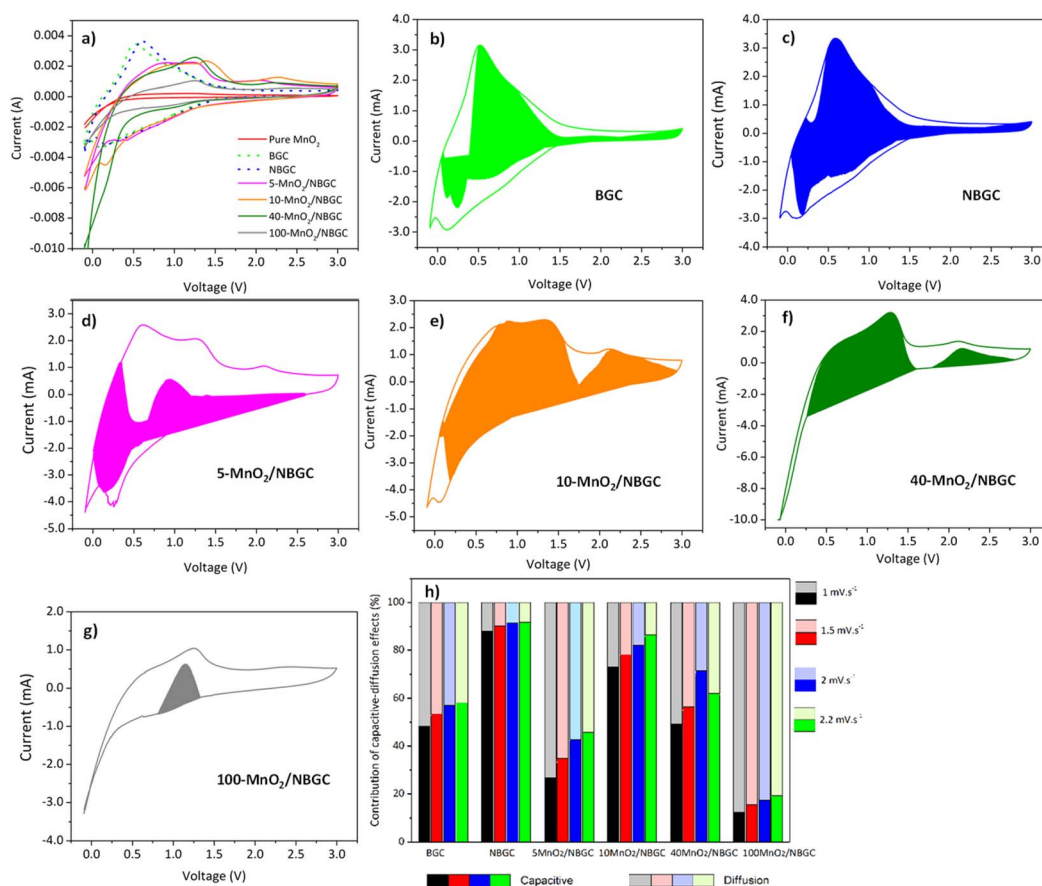


**Fig. 6** (a) Cyclic voltammograms (CVs) of BGC, NBGC and  $\text{MnO}_2/\text{NBGC}$  composite at various  $\text{MnO}_2$  loading contents at  $2 \text{ mV s}^{-1}$ , CVs at scan rates of  $2 \text{ mV s}^{-1}$  and the corresponding capacitive currents (colored region) of (b) BGC, (c) NBGC, (d) 5- $\text{MnO}_2/\text{NBGC}$ , (e) 10- $\text{MnO}_2/\text{NBGC}$ , (f) 40- $\text{MnO}_2/\text{NBGC}$ , (g) 100- $\text{MnO}_2/\text{NBGC}$ , and (h) capacity contribution ratios at various scan rates of BGC, NBGC and  $\text{MnO}_2/\text{NBGC}$  composite at various  $\text{MnO}_2$  loading contents.





Furthermore, the lithium-ion storage mechanisms of BGC, NBGC, and the  $\text{MnO}_2/\text{NBGC}$  composites with different doping content were investigated by using cyclic voltammetry to observe their electrochemical behavior at varied scanning rates. The relationship between the current and the scanning rate is depicted by the following eqn (5),<sup>38–41</sup> and the charge storage process is also described by eqn (5).

$$i = av^b \quad (5)$$

where the measured current  $i$  follows the power law relationship with the scan rate  $v$ . Both  $a$  and  $b$  are fitting parameters obtained from the intercept and slope of the plot  $\log(i)$  vs.  $\log(v)$ , respectively. There are two defined values for  $b$ , *i.e.* 0.5 and 1.0. At  $b = 0.5$ , the current is proportional to the square root of the sweep rate  $v$ , and the current response is purely controlled by ion diffusion in the electroactive material, reflecting that the current and capacity result from the faradaic intercalation/extraction processes. Meanwhile, at  $b = 1.0$ , the current is linearly proportional to the sweep rate  $v$ , which is considered capacitive response; here, the current and capacity originate from the charge-transfer process involving the surface atoms and the non-faradaic double layer effect or surface adsorption process. Therefore, for a system governed by the synergistic effect between ionic diffusion and the surface capacitive effect, the relationship between the current and the scan rate at a fixed potential can be described as follows:

$$I(V) = k_1v + k_2v^{1/2} \quad (6)$$

$$I(V)/v^{1/2} = k_1v^{1/2} + k_2 \quad (7)$$

where both  $k_1$  and  $k_2$  are constants at each fixed potential, while  $k_1v$  and  $k_2v^{1/2}$  correspond to the current contributions of the surface capacitive effects and diffusion-controlled intercalation/extraction processes, respectively. To quantitatively estimate the current contributions of the surface capacitive effects and diffusion-controlled insertion/extraction processes, a series of  $k_1$  and  $k_2$  for each potential was solved by plotting  $I(V)/v^{1/2}$  vs.  $v^{1/2}$ , in which the slope and y-axis intercept of the plot correspond to  $k_1$  and  $k_2$ , respectively. The ratio of capacitive contribution to the total capacity was determined from the integrated area of the plot ( $k_1v$  vs. potential) and the total integrated area of the CV curve. Fig. S3a–f† show the CVs of BGC, NBGC and  $\text{MnO}_2/\text{NBGC}$  doped with different loadings of  $\text{MnO}_2$  at various sweep rates between 0.1 and 2.2  $\text{mV s}^{-1}$ , respectively. It can be observed that all anodic peaks had shifted to higher potentials, and the cathodic peaks moved to lower potentials with the increase in scanning rate. This reflects high polarization at high sweep rates. Fig. 6b–g present the ratios of capacitive contribution to the total capacity obtained by integrating the area of capacitive current ( $k_1v$ ) vs. potential curve in comparison with the total area of the CV curves at the selected scan rates of

2  $\text{mV s}^{-1}$ . While, the capacity contribution ratios between capacitive effect to the diffusion controlled process are summarized in Fig. 6h. The values of  $k_1$  and  $k_2$  at various potentials were calculated by employing eqn (7). Regarding the behavior, the samples were classified into two groups, namely (i) BGC and NBGC and (ii) the  $\text{MnO}_2/\text{NBGC}$  composites with various  $\text{MnO}_2$  contents, to analyze the kinetics of the ionic storage mechanism. For BGC and NBGC, the capacities mainly depended on the surface capacitive effect, as indicated by the high capacitive contribution, that is, roughly more than half, including 48–53% for BGC and 88–92% for NBGC. The high capacitive contributions may be attributed to the high surface area of the materials. Especially, the significantly high capacitive contribution (more than 80%) in the case of NBGC may result from its abundant exposed electron rich-N functional groups that readily attract the lithium ions. Compared with their parent, *i.e.* NBGC, the  $\text{MnO}_2/\text{NBGC}$  composites showed less influence of the capacitive effect on their capacities. With the addition of  $\text{MnO}_2$ , it was clearly seen that the ionic storage mechanism was increasingly controlled by the synergistic impact of the surface capacitive effect and diffusion-controlled insertion/extraction processes. The capacitive contributions of the  $\text{MnO}_2/\text{NBGC}$  composites at varying scan rates ranging from 1–2.2  $\text{mV s}^{-1}$  were 27–46%, 73–86%, 49–71%, and 12–19%, for 5- $\text{MnO}_2/\text{NBGC}$ , 10- $\text{MnO}_2/\text{NBGC}$ , 40- $\text{MnO}_2/\text{NBGC}$ , and 100- $\text{MnO}_2/\text{NBGC}$ , respectively. Interestingly, with the increase in  $\text{MnO}_2$  doping, the ionic capacity seemed to basically rely on the capacitive effect or adsorption at the surface of the active  $\text{MnO}_2/\text{NBGC}$  electrode composites up to an optimum condition. With a further increase in  $\text{MnO}_2$  doping, the ionic storage process predominantly depended on ionic diffusion-controlled intercalation/extraction to the crystalline structure of the active material. Notably, 5- $\text{MnO}_2/\text{NBGC}$ , which had a comparable specific surface area and N content but a relatively lower amount of  $\text{MnO}_2$  than 10- $\text{MnO}_2/\text{NBGC}$  (see Tables 1 and S1†), showed quite a low capacitive contribution. The reason for the greater role of the diffusion-controlled process in the case of the 5- $\text{MnO}_2/\text{NBGC}$  sample may be the better crystallinity of its structure as it was grown with a more diluted  $\text{KMnO}_4$  precursor. A high initial  $\text{KMnO}_4$  concentration may cause very rapid growth of  $\text{MnO}_2$  crystals on the carbon surface, leading to the formation of  $\text{MnO}_2$  nanocrystals with denser or lower crystallinity. Hence, 5- $\text{MnO}_2/\text{NBGC}$ , which has a better crystalline structure of the  $\text{MnO}_2$  active material, would better support the process of  $\text{Li}^+$  intercalation/extraction. This can promote its ionic capacity thereby high storage capability of the  $\text{MnO}_2$  compound. The 10- $\text{MnO}_2/\text{NBGC}$  sample, which possesses lower  $\text{MnO}_2$  crystallinity while holding a comparable surface area to 5- $\text{MnO}_2/\text{NBGC}$ , would then prefer ionic storage *via* surface adsorption processes. Further increasing  $\text{MnO}_2$  doping on the NBGC, as the cases of 40- $\text{MnO}_2/\text{NBGC}$  and 100- $\text{MnO}_2/\text{NBGC}$ , did not only reduce the specific surface area due to blockage of the porous structure, but the thick  $\text{MnO}_2$  coating would also shield the exposed N-functional groups on NBGC. In addition, their  $\text{MnO}_2$  nanocrystallites may exhibit low crystallinity under a dense crystalline growth. This may result in a lower capacitive contribution to the ionic capacity and also low capacity due to





limited ionic intercalation in the poor crystalline structures. In particular, 100-MnO<sub>2</sub>/NBGC, which contained a substantially high MnO<sub>2</sub> content while possessing the lowest surface area, acted more like bulk MnO<sub>2</sub>, thereby favoring an ionic storage mechanism *via* the intercalation/extraction processes. Moreover, the fraction of capacitive contribution to the total capacity of all the MnO<sub>2</sub>/NBGC composites mostly increased with the scanning rate and current density (Fig. 6h), indicating that at high charge/discharge rates, they are likely to rely on the surface capacitive effect or surface adsorption process to sustain their ionic capacity. The high contribution of pseudocapacitance

would be beneficial to the electrochemical performance of electroactive materials at high rate capacities.

The voltage profiles of BGC, NBGC and the MnO<sub>2</sub>/NBGC composites at a current density of 186 mA g<sup>-1</sup> (approximately 0.5C based on the theoretical capacity of graphite, ~370 mA h g<sup>-1</sup> as the reference) in the 1st, 2nd and 50th cycles are presented in Fig. 7. For BGC and NBGC, only a sloped discharge potential, as generally found in carbon-based electrodes, could be observed. In the case of the MnO<sub>2</sub>/NBGC composites, an obvious plateau was observed at around 0.45 V in the discharge process, corresponding to the reduction of Mn<sup>4+</sup> to Mn<sup>0</sup>. In the charging process, the sloped potentials at around 1.51 V and 2.25 V were ascribed to the two steps of Mn oxidation, in agreement with the CV scan result. It was found that the composites with greater MnO<sub>2</sub> loadings (such as 40-MnO<sub>2</sub>/NBGC and 100-MnO<sub>2</sub>/NBGC) exhibited similar characteristics to pure MnO<sub>2</sub>, where the long plateau potential at 0.45 V was obviously observed. The 1st cycle discharge capacities of most MnO<sub>2</sub>/NBGC composites were higher than the theoretical capacity of MnO<sub>2</sub> (1230 mA h g<sup>-1</sup>), reflecting the mixed processes of ionic storage. The extreme decay of the specific capacity in the 2nd cycle resulted from the formation of the SEI due to the decomposition of the electrolyte at the electrode interface during the 1st discharge process. The formation of the coating layer limits ionic accessibility to the electrode in the subsequent cycles.<sup>36</sup> This irreversible capacity from the first cycle is highly dependent on the mobility of Li<sup>+</sup> and e<sup>-</sup> during the Li extraction process. Li<sup>+</sup> transport can be enhanced by the formation of a nanoporous SEI structure at the end of the first discharge cycle that can facilitate the penetration of the electrolyte into the nanopores of the electrode. However, electron transport in the electrode may not be affected since the electrolyte cannot supply free electrons to the electrode. Therefore, electron mobility is highly dependent on the original particle size. In the following cycles, charging and discharging were quite reversible due to the stability of the SEI microstructure after several cycles. After 50 cycles, only the MnO<sub>2</sub>/NBGC composites with medium to low MnO<sub>2</sub> loadings, namely 5-MnO<sub>2</sub>/NBGC and 10-MnO<sub>2</sub>/NBGC, exhibited high capacity retention of more than 90% relative to the capacity obtained in the 2nd cycle.

As shown in Fig. 8, the cycling performances of the bagasse-derived carbon anode material and its composites with various MnO<sub>2</sub> loadings were compared with that of pure MnO<sub>2</sub> nanoparticles to explore the benefit of the doped N-functional groups and the MnO<sub>2</sub> nanoparticles dispersed on the carbon porous substrate, as well as the impact of the MnO<sub>2</sub> coating layer on the corresponding electrochemical performance. As shown in Fig. 8a, the half-cell tests were cycled between 0 and 3 V at a current density of 186 mA g<sup>-1</sup> for 50 cycles. The initial capacity of the parent carbon materials, namely BGC and NBGC, the doped MnO<sub>2</sub>/NBGC composites, including 5-MnO<sub>2</sub>/NBGC, 10-MnO<sub>2</sub>/NBGC, 40-MnO<sub>2</sub>/NBGC, and 100-MnO<sub>2</sub>/NBGC, and the pure synthesized MnO<sub>2</sub> were 815, 1016, 1394, 1348, 1265, 1232 and 1450 mA h g<sup>-1</sup>, respectively. These obtained capacities were higher than the theoretical capacities of graphite and the MnO<sub>2</sub> crystalline material, reflecting the combination of the ionic

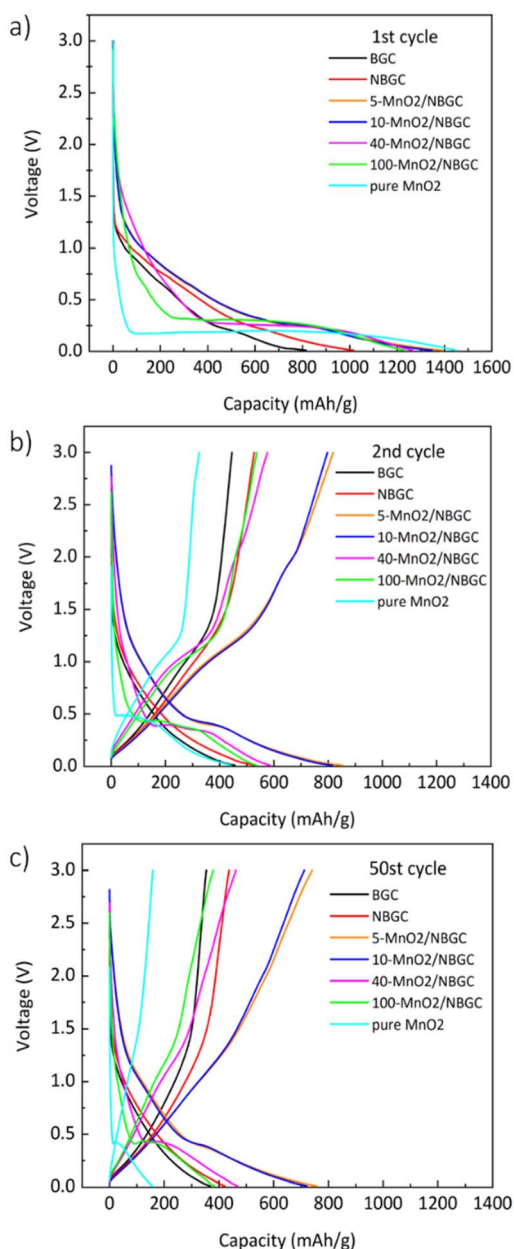


Fig. 7 The voltage profiles of bagasse-derived carbon material (BGC), N-doping bagasse-derived carbon (NBGC), and MnO<sub>2</sub>/NBGC composites with various MnO<sub>2</sub> loadings at the (a) 1st cycle, (b) 2nd cycle, and (c) 50th cycle.



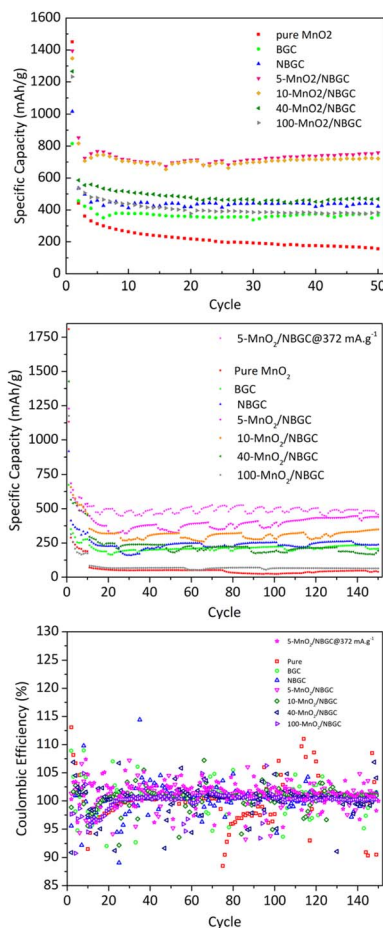


Fig. 8 Cycling performance of BGC, NBGC,  $\text{MnO}_2/\text{NBGC}$  at various  $\text{MnO}_2$  loadings and pure synthesized  $\text{MnO}_2$ : (a) cycling at a current density of  $186 \text{ mA g}^{-1}$ , (b) cycling at a current density of  $774 \text{ mA g}^{-1}$  and (c) their corresponding coulombic efficiency at a current density of  $774 \text{ mA g}^{-1}$ .

storage mechanisms. In the 2nd cycle, all samples had substantial capacity decay reaching  $457, 535, 853, 816, 586, 536$ , and  $442 \text{ mA h g}^{-1}$ , respectively. This capacity decay typically results from the influence of SEI formation. However, all samples showed great coulombic efficiencies of almost 100% during the 50-cycle tests. Regarding the reduction in carbon content with increasing  $\text{MnO}_2$  doping amount (see Table S1<sup>†</sup>), the obtained capacities of the  $\text{MnO}_2/\text{NBGC}$  composites were quite dependent on the  $\text{MnO}_2$  compound. After 50 cycles, all  $\text{MnO}_2/\text{NBGC}$  composites with different  $\text{MnO}_2$  loading concentrations and even the un-doped bagasse-based carbon materials exhibited much better cycling performance than that of the pure  $\text{MnO}_2$  electrode. After 50 cycles,  $5\text{-MnO}_2/\text{NBGC}$ ,  $10\text{-MnO}_2/\text{NBGC}$ ,  $40\text{-MnO}_2/\text{NBGC}$ , and  $100\text{-MnO}_2/\text{NBGC}$  could retain specific capacities of  $759, 722, 468$ , and  $382 \text{ mA h g}^{-1}$ , which correspond to about 54%, 54%, 37%, and 31% capacity retention, respectively. Meanwhile, the parent porous carbon substrates NBGC and BGC exhibited specific capacities of  $422$  and  $368 \text{ mA h g}^{-1}$ , demonstrating capacity retention of 45% and 42%, respectively. Although the pure  $\text{MnO}_2$  electrode expressed a very high initial capacity ( $\sim 1450 \text{ mA h g}^{-1}$ ), its 2nd cycle

capacity considerably dropped and continually decreased through the end of the 50th cycle, finally holding a specific capacity of only  $156 \text{ mA h g}^{-1}$ , corresponding to 11% retention. This clearly reveals the dramatic instability of the bulk pure  $\text{MnO}_2$  compound. Compared with their parent substrates (*i.e.* NBGC and BGC) and pure  $\text{MnO}_2$ , the superior capacity of the  $\text{MnO}_2/\text{NBGC}$  composites reflects the influence of the high-capacity  $\text{MnO}_2$  active compound in addition to the capacitive effect of the N-functional groups and the large surface area of the parent carbon substrate. However, the composite samples that contained a high density of deposited  $\text{MnO}_2$ , such as  $40\text{-MnO}_2/\text{NBGC}$  and  $100\text{-MnO}_2/\text{NBGC}$ , behaved more like the bulk  $\text{MnO}_2$ , hence displaying significantly lower capacity than the samples with less  $\text{MnO}_2$  doping, namely  $5\text{-MnO}_2/\text{NBGC}$  and  $10\text{-MnO}_2/\text{NBGC}$ . Relative to the capacity observed in the 2nd cycle, where the formed SEI layer was quite stable, the samples BGC, NBGC,  $5\text{-MnO}_2/\text{NBGC}$ ,  $10\text{-MnO}_2/\text{NBGC}$ ,  $40\text{-MnO}_2/\text{NBGC}$ ,  $100\text{-MnO}_2/\text{NBGC}$ , and pure  $\text{MnO}_2$  demonstrated 81%, 79%, 89%, 88%, 80%, 71%, and 35% capacity retention, respectively. All the bagasse-based electrodes exhibited high capacity retention above  $\sim 80\%$ , except for pure  $\text{MnO}_2$ , which still showed low retention of about 35%. The poor cycling stability of the pure  $\text{MnO}_2$  electrode is attributed to its typically large volume expansion, which causes weaker adhesion with the current collector after several cycling tests.<sup>16</sup> Considering the impact of the  $\text{MnO}_2$  coating amount on the electrochemical performance of the composite electrodes, increasing the  $\text{MnO}_2$  loading amount either led to a reduction in the specific capacity of the composites or resulted in  $\text{MnO}_2$  structures with poor crystallinity due to the dense crystalline growth. With thin  $\text{MnO}_2$  coatings, the  $5\text{-MnO}_2/\text{NBGC}$  and  $10\text{-MnO}_2/\text{NBGC}$  samples exhibited high performance because of the synergistic effect of the high-capacity  $\text{MnO}_2$  active material and the supported capacitive effect arising from the exposed N-containing defects. In addition, the thin coating allowed better adhesion of  $\text{MnO}_2$  with the carbon surface and could better tolerate the high stress from its large expansion. In contrast, thick  $\text{MnO}_2$  coatings, as found in the  $40\text{-MnO}_2/\text{NBGC}$  and  $100\text{-MnO}_2/\text{NBGC}$  samples, would not only block the pore channels of the parent carbon material, leading to a reduction in the specific surface area but also would shield the capacitive effect of the N-containing functional groups on the carbon substrate from the contacting electrolyte. In addition, the low crystalline quality resulting from rapid crystalline growth at high concentrations of  $\text{MnO}_2$  would limit the diffusion-controlled intercalation/extraction process of  $\text{Li}^+$  through the  $\text{MnO}_2$  compound. Large  $\text{MnO}_2$  agglomerates would also result in weak adhesion with the substrate and may generate non-uniform expansion during cycling, causing instability or detachment of some  $\text{MnO}_2$  coatings after several cycles. To evaluate the long-term cyclic performance of the  $\text{MnO}_2/\text{NBGC}$  electrode materials, their as-assembled LIBs were cycled at  $774 \text{ mA g}^{-1}$  ( $\sim 2C$  based on the theoretical capacity of graphite with  $\sim 370 \text{ mA h g}^{-1}$  as the reference) for 150 cycles, as depicted in Fig. 8b. The cells assembled from  $5\text{-MnO}_2/\text{NBGC}$ ,  $10\text{-MnO}_2/\text{NBGC}$ ,  $40\text{-MnO}_2/\text{NBGC}$ ,  $100\text{-MnO}_2/\text{NBGC}$ , NBGC, BGC, and pure synthesized  $\text{MnO}_2$  exhibited average reversible discharge capacities of



390.03, 306.94, 211.63, 66.29, 233.32, 208.11 and 43.05 mA h g<sup>-1</sup>, respectively. All samples showed great reversibility with the coulombic efficiency reaching nearly 100%, as shown in Fig. 8c. The observed long-term capacity behaviour at high rates also confirms the synergistic influence of the high-capacity MnO<sub>2</sub> compound and the pseudocapacitive effect arising from the N-containing defects and the large surface area, as previously mentioned. For instance, the composite comprising a thin MnO<sub>2</sub> coating exhibited high storage capability compared to the samples that were coated with thick MnO<sub>2</sub> layers. It was found that even at a relatively high current density, 5-MnO<sub>2</sub>/NBGC exhibited a specific capacity of 390 mA h g<sup>-1</sup> (487.6 mA h g<sup>-1</sup> at 372 mA g<sup>-1</sup>), which is higher than the capacity of typical graphite (~370 mA h g<sup>-1</sup>). Thicker MnO<sub>2</sub> coating layers at elevated MnO<sub>2</sub> doping levels resulted in declined ionic capacity. Interestingly, the 100-MnO<sub>2</sub>/NBGC sample with a very thick MnO<sub>2</sub> coating exhibited a substantial drop in capacity, even lower than that of BGC, which is the carbon material without N-doping. Moreover, it behaved more like the bulk pure MnO<sub>2</sub> instead of the MnO<sub>2</sub>/NBGC carbon composite, delivering a comparatively low capacity as the

unstable MnO<sub>2</sub>. The high pseudocapacitive effect in NBGC, which does not hold a MnO<sub>2</sub>, could promote high rate capability, leading to a higher specific capacity than that of the 40-MnO<sub>2</sub>/NBGC sample.

As shown in Fig. 9, different current densities were applied to investigate the rate performance of the MnO<sub>2</sub>/NBGC samples with various MnO<sub>2</sub> loadings and compared with their parent bagasse-derived porous carbons (NBGC and BGC), as well as, the synthesized pure MnO<sub>2</sub>. Different current densities, including 74.4 mA g<sup>-1</sup>, 186 mA g<sup>-1</sup>, 372 mA g<sup>-1</sup>, 1860 mA g<sup>-1</sup>, 3720 mA g<sup>-1</sup>, which are approximately equivalent to about 0.2C, 0.5C, 1C, 5C, and 10C, respectively, (based on the 1C graphite theoretical capacity of about 372 mA g<sup>-1</sup>) were consecutively applied for 10 cycles, 10 cycles, 10 cycles, 50 cycles, and 50 cycles, respectively, and eventually restored back to 74.4 mA g<sup>-1</sup> for 10 cycles. As summarized in Table 2, all samples exhibited good rate performance, achieving great capacity retention of more than 70% even under high applied current densities of 1860 mA g<sup>-1</sup> and 3720 mA g<sup>-1</sup> over almost 100 cycles. Compared with the MnO<sub>2</sub> composite samples, pure MnO<sub>2</sub> exhibited poor reversibility with quite a low capacity retention of ~59%. Similar to the trend achieved in the cycling performance assessment, regarding the synergistic impact of the inserted high-capacity MnO<sub>2</sub> compound and N-doping, the MnO<sub>2</sub>/NBGC composite samples with low to medium MnO<sub>2</sub> loadings, namely the 5-MnO<sub>2</sub>/NBGC and 10-MnO<sub>2</sub>/NBGC composites, displayed distinctively great rate performances. Interestingly, 5-MnO<sub>2</sub>/NBGC could deliver a high specific capacity of up to 388 and 301 mA h g<sup>-1</sup> at high current densities of 1860 and 3720 mA g<sup>-1</sup>, or about 5C and 10C, respectively. At low to relatively high current densities (74.4–1860 mA g<sup>-1</sup>), though exhibited comparable performance 10-MnO<sub>2</sub>/NBGC was found to exert a slightly higher capacity than 5-MnO<sub>2</sub>/NBGC. This may imply its favorable thermodynamics-controlled ionic storage at low current density due to higher MnO<sub>2</sub> doping. However, when tested at a very high current density of 3720 mA g<sup>-1</sup>, 5-MnO<sub>2</sub>/NBGC showed distinctively higher capacity than 10-MnO<sub>2</sub>/NBGC. Their comparable performance at low to medium current densities may be attributed to their similar specific surface area and comparable amounts of N-containing groups, which support the accessibility of the electrolyte to the electrode material and promote the pseudo capacitive effect. However, higher amounts of loaded MnO<sub>2</sub> may

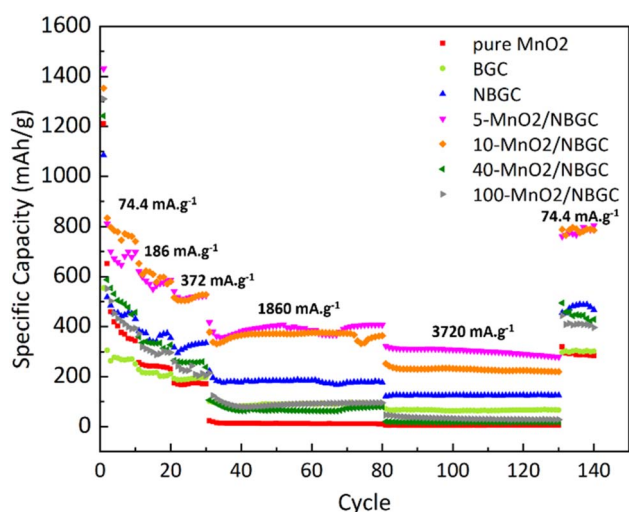


Fig. 9 Rate performance of bagasse-derived carbon material (BGC), N-doping bagasse-derived carbon (NBGC), MnO<sub>2</sub>/NBGC carbon composite with various MnO<sub>2</sub> loading concentrations and the pure hydrothermally synthesized MnO<sub>2</sub>.

Table 2 The specific capacity of bagasse-derived carbon material and its composites with different MnO<sub>2</sub> loadings under varying current density

Carbon composite	Average specific capacity at varied current densities (mA h g <sup>-1</sup> )						Capacity retention (%)
	74.4 (mA g <sup>-1</sup> )	186 (mA g <sup>-1</sup> )	372 (mA g <sup>-1</sup> )	1860 (mA g <sup>-1</sup> )	3720 (mA g <sup>-1</sup> )	74.4 (mA g <sup>-1</sup> )	
Pure MnO <sub>2</sub>	493	242	171	12	4	292	59
BGC	300	212	192	89	65	301	100
NBGC	521	363	321	183	125	475	91
5-MnO <sub>2</sub> /NBGC	767	580	519	388	301	780	101
10-MnO <sub>2</sub> /NBGC	833	603	514	365	228	784	94
40-MnO <sub>2</sub> /NBGC	578	332	256	77	17	447	77
100-MnO <sub>2</sub> /NBGC	526	308	225	93	32	410	77





form thicker coating layers that shield the exposed N-functional groups on the carbon substrate and drive poor  $\text{MnO}_2$  crystalline growth. In addition, depositing  $\text{MnO}_2$  at higher  $\text{KMnO}_4$  concentrations may increase the dispersion of the  $\text{MnO}_2$  clusters, leading to lower dimensional stability because of their non-uniform and large volume expansion under high current densities, such as  $3720 \text{ mA g}^{-1}$ . Both 5- $\text{MnO}_2$ /NBGC and 10- $\text{MnO}_2$ /NBGC showed great reversibility with high capacity retention of more than 90% and even full recovery in the case of 5- $\text{MnO}_2$ /NBGC, when restored back to the low rate of  $74.4 \text{ mA g}^{-1}$ . Notably, such high-capacity compound  $\text{MnO}_2$  seems to play a greater role than the surface capacitive effect when operated under low current densities, such as  $74.4 \text{ mA g}^{-1}$ . However, the higher specific capacity of NBGC than those of the high  $\text{MnO}_2$ -loaded composites, such as 40- $\text{MnO}_2$ /NBGC and 100- $\text{MnO}_2$ /NBGC, at high current densities suggests a major impact of the capacitive effect arising from the doped N-containing groups, as well as, the large surface area on the ionic conduction and stability of the  $\text{MnO}_2$  coating layer to sustain the capacity at high rates. In agreement with the results from the cycling test, thick  $\text{MnO}_2$  coating layers may not be able to tolerate large dimensional changes under fast rates and cause weak adhesion, leading to a dramatic capacity drop possibly due to the detachment of  $\text{MnO}_2$  from the carbon substrate.

The electrochemical impedances of BGC, NBGC, 5- $\text{MnO}_2$ /NBGC, 10- $\text{MnO}_2$ /NBGC, 40- $\text{MnO}_2$ /NBGC and 100- $\text{MnO}_2$ /NBGC were analyzed by using electrochemical impedance spectroscopy (EIS) in the frequency range of 0.1–100 000 Hz and

a voltage of 10 mV, as illustrated in Fig. 10a. Based on the electrical equivalent circuit (EEC) shown as the inset, all the Nyquist plots composed of a single semicircle in the high-to-medium frequency range and a diagonal inclined line in the middle-to-low frequency range, corresponding to the charge transfer resistance ( $R_{\text{ct}}$ ) and lithium ionic diffusion ability, respectively. The electrochemical charge transfer resistance ( $R_{\text{ct}}$ ) of each sample was obtained from the extrapolated intercept of the semicircle plot in the medium-frequency range on the X-axis. The electrochemical impedance generally reflects the ion transport ability within the bulk electrolyte through the electrode material. In particular, the charge transfer resistance denotes the transport of ions through the interface between the electrode material and electrolyte solution. BGC, NBGC, 5- $\text{MnO}_2$ /NBGC, 10- $\text{MnO}_2$ /NBGC, 40- $\text{MnO}_2$ /NBGC, and 100- $\text{MnO}_2$ /NBGC revealed  $R_{\text{ct}}$  values of 65.2, 46.1, 33.2, 38.5, 41.0 and 57.5 ohms, respectively. These can be ranked as  $R_{\text{ct}}$  (5- $\text{MnO}_2$ /NBGC) <  $R_{\text{ct}}$  (10- $\text{MnO}_2$ /NBGC) <  $R_{\text{ct}}$  (40- $\text{MnO}_2$ /NBGC) <  $R_{\text{ct}}$  (NBGC) <  $R_{\text{ct}}$  (100- $\text{MnO}_2$ /NBGC) <  $R_{\text{ct}}$  (BGC). This ionic conduction trend is quite consistent with that of their specific capacities. Moreover, it is most likely influenced by the crystallinity of the doped  $\text{MnO}_2$  nanoclusters and the specific surface area. For instance, a better crystalline structure when combined with a large specific surface area tends to promote higher ionic conduction. Furthermore, the reduction in ionic conductivity of the  $\text{MnO}_2$ /NBGC electrode after cycling at  $774 \text{ mA g}^{-1}$  for 150 cycles was explored by TEM and the EIS of representative carbon composite electrode materials, namely NBGC, 5- $\text{MnO}_2$ /NBGC, and 100- $\text{MnO}_2$ /NBGC, as illustrated in Fig. 10c–e. The Nyquist

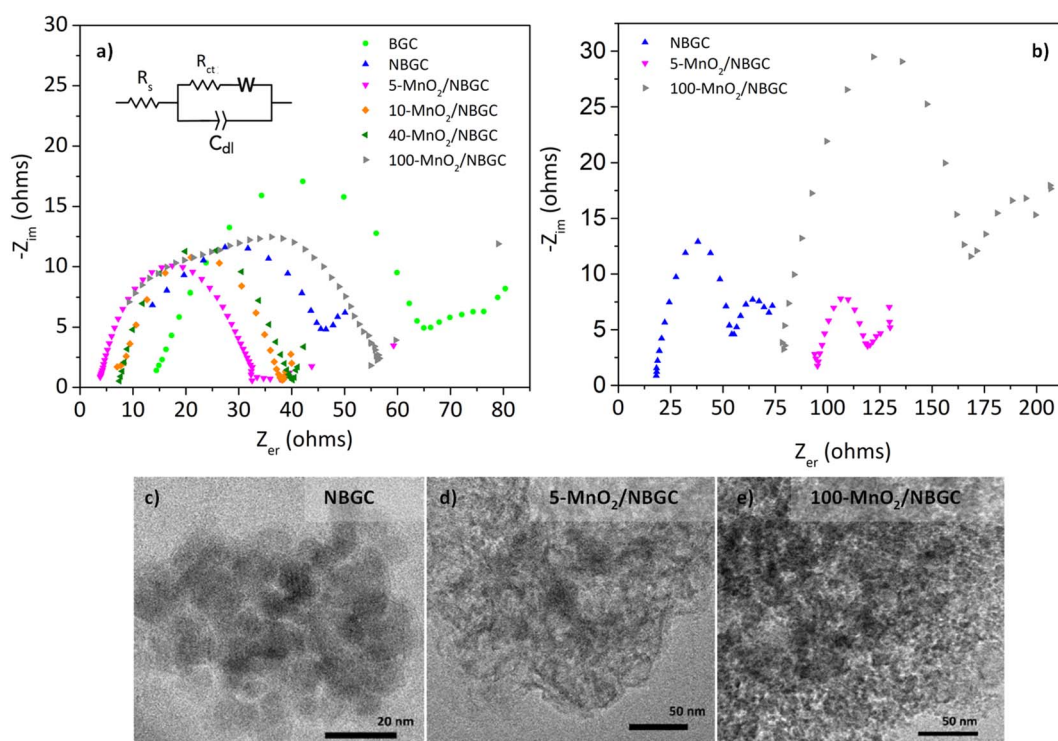


Fig. 10 Electrochemical impedance of (a) the fresh carbon composite anode electrodes and (b) carbon composite anode electrodes after cycling at  $774 \text{ mA g}^{-1}$  for 150 cycles; the TEM images of some spent carbon composite electrodes: (c) NBGC, (d) 5- $\text{MnO}_2$ /NBGC, and (e) 100- $\text{MnO}_2$ /NBGC.

plots of the used electrode material seemed to depict an additional second semicircle at medium frequencies, reflecting the formation of a secondary phase or additional resistance generated after the cycling tests. They also showed higher charge transfer resistances compared with the fresh electrodes and could be arranged as  $R_{ct}$  (NBGC)  $< R_{ct}$  (5-MnO<sub>2</sub>/NBGC)  $< R_{ct}$  (100-MnO<sub>2</sub>/NBGC). A comparison of the TEM images of the spent electrodes relative to the fresh ones depicted in Fig. 2 revealed that the NBGC and 5-MnO<sub>2</sub>/NBGC electrode materials did not clearly show morphology changes, whereas, the obvious flaky structure of the MnO<sub>2</sub> coating layer for the 100-MnO<sub>2</sub>/NBGC sample disappeared after long cycling. This may imply the degradation of the unstable thick MnO<sub>2</sub> coating layer due to non-uniform expansion during cycling, eventually leading to its detachment from the porous carbon substrate and causing large resistance due to the collapse of the crystalline structure.

Table 3 demonstrates the comparison of previously reported electrochemical performances of manganese oxide compound/carbon composites in various fabricated structures. Most of the developed manganese oxide/carbon composite electrodes exhibited a capacity of more than 400 mA h g<sup>-1</sup>, which is higher

than the theoretical capacity of the typical graphite electrode. This may be attributed to the utilization of carbon nanotubes or graphene sheets as the highly conductive carbon substrate with enhanced specific surface for the nanocrystalline growth of high-capacity manganese oxide compounds. However, though porous graphene or carbon nanotubes deliver high ionic capacity at high current densities, the materials are expensive and require elaborate fabricating methods. In comparison with the manganese oxide/carbon composite electrodes from previous studies, our best sample 5-MnO<sub>2</sub>/NBGC delivers quite a high reversible capacity ( $\sim 722$  mA h g<sup>-1</sup> at a moderate current density of 186 mA g<sup>-1</sup>,  $\sim 0.5C$  based on theoretical graphite capacity). Moreover, it shows relatively high capacity and good stability at high current densities: 488 at 372 mA g<sup>-1</sup>, and 390 at 744 mA g<sup>-1</sup>. This great storage capability may arise from the synergistic effect of the stable MnO<sub>2</sub> nanocrystalline structures deposited onto the porous carbon substrate with enhanced surface area containing high-capacitive N-functional groups. In addition, the appropriate density of the MnO<sub>2</sub> nanocrystalline particles on the porous substrate promotes the formation of good crystalline and optimizes the obtained specific surface

**Table 3** Comparison of the electrochemical performance of various composites of manganese oxide compounds and carbon materials

Sample	Material	Specific capacity (mA h g <sup>-1</sup> )	Potential range (V)	References
MnO <sub>2</sub> /CNT	Composite of coated MnO <sub>2</sub> nanoflakes on connected carbon nanotubes	620 at 200 mA g <sup>-1</sup> after 50 cycles	0.01–3	16
$\alpha$ -MnO <sub>2</sub> /GNS	Composite of $\alpha$ -MnO <sub>2</sub> nanosheets distributed on graphene surface	693.7 at 0.05C and 387.7 at 0.2C after 30 cycles	0.01–3	34
MnO <sub>2</sub> /CNTs	Composite of hybrid coaxial structured MnO <sub>2</sub> and carbon nanotubes	500 at 50 mA g <sup>-1</sup> after 15 cycles	0.02–3.2	36
C/MnO-L	Composite of commercial MnO coated with sugar-derived carbon material	400 at 400 mA g <sup>-1</sup>	0.01–3	42
N-MnO/GNS	Composite of N-doped MnO distributed on graphene nanosheets	772 at 100 mA g <sup>-1</sup> after 90 cycles	0–3	43
MnO@C core-shell nanoplates	Composite of core-shell MnO nanoplates coated with carbon material	770 at 200 mA g <sup>-1</sup> after 30 cycles	0.001–3	44
MnO <sub>2</sub> /CNHs	Composite of MnO <sub>2</sub> nanoflakes coated on carbon nanohorns (CNHs)	565 at 100 mA g <sup>-1</sup> after 60 cycles	0.05–3	45
MnO <sub>2</sub> NFs@GF	Interconnected MnO <sub>2</sub> nanoflakes (NFs) assembled on CVD-grown graphene (GF) foam	1200 mA h g <sup>-1</sup> at 500 mA g <sup>-1</sup> after 300 cycles and 500 mA h g <sup>-1</sup> at 5 A g <sup>-1</sup>	0.01–3.00	46
GMG	Composite of graphene-coated MnO <sub>2</sub> deposited on graphene nanoribbons (GNRs)	612 mA h g <sup>-1</sup> at 400 mA g <sup>-1</sup> after 250 cycles	0.01–3.00	47
MnO <sub>2</sub> nanotube/graphene	Thin film composites of layered-by-layered graphene and MnO <sub>2</sub> nanotubes	495 mA h g <sup>-1</sup> at 100 mA g <sup>-1</sup> after 40 cycles	0.01–3.00	48
5-MnO <sub>2</sub> /NBGC	Composite of dispersed MnO <sub>2</sub> nanoparticles on the N-doped bagasse-derived porous carbon material	722 at 186 mA g <sup>-1</sup> after 50 cycles, 488 at 372 mA g <sup>-1</sup> after 150 cycles, and 390 at 744 mA g <sup>-1</sup> after 150 cycles	0.01–3	This work



area of the composite products. The proposed utilization of agricultural wasted sugarcane bagasse, might promote the concept of using sustainable raw materials to produce a higher-value electrode material for electrochemical storage devices that can sustain comparable performance to expensive electrode materials.

To further align the academic and industrial practices for the potential utilization of our proposed 5-MnO<sub>2</sub>/NBGC anode material, the energy density of the full-cell fabricated using 5-MnO<sub>2</sub>/NBGC coupled with an LFP cathode was calculated based on the method presented by Son *et al.*<sup>49</sup> The calculated full-cell energy density was then compared with the case where the common graphite anode material was employed. The calculated results for both cases are illustrated in Fig. S4.† Basically, the energy density of the full cell mainly relies on the practical capacity of the cathode material and the nominal voltage between the cathode and the anode. The nominal voltage of the full cell may be roughly approximated from the potential difference between the plateau voltages derived from separate half-cell GCD tests of each cathode and anode material *vs.* Li/Li<sup>+</sup>. With the same cathode material, the anode material which provides lower voltage may gather a higher output of nominal voltage when coupled in the full cell. Based on the energy density calculation shown in ESI,† with the same electrode mass loading, the calculated full-cell energy densities for the LFP-5MnO<sub>2</sub>/NBGC and LFP-graphite electrode couples were 137.42 and 151.16 A h kg<sup>-1</sup>, respectively. The lower full-cell energy density of the LFP-5MnO<sub>2</sub>/NBGC couple compared to that of the LFP-graphite pair results from its higher half-cell testing nominal voltage (0.45 V) relative to 0.15 V for typical graphite. Though it is predicted to deliver slightly lower full cell energy density compared with the common graphite anode, 5-MnO<sub>2</sub>/NBGC showed quite an impressive rate performance (*i.e.* 388 mA h g<sup>-1</sup> at a current density of 1860 mA g<sup>-1</sup>, approximately 5C) and good cycling stability. This promising rate performance and cycling stability of 5-MnO<sub>2</sub>/NBGC may promote its potential usage in batteries for fast-rate applications and ensure a longer lifetime.

## Conclusions

Composites of the N-doped bagasse-derived porous carbon with dispersed MnO<sub>2</sub> nanoparticles (MnO<sub>2</sub>/NBGC) were fabricated *via* a practical method. Controlled loading of MnO<sub>2</sub> nanoparticles on the porous carbon substrate could be achieved by varying the KMnO<sub>4</sub> precursor concentration in the reduction reaction. Increasing the MnO<sub>2</sub> loading content caused the formation of thick flake-like MnO<sub>2</sub> coating layers on the porous carbon surface, leading to a reduction in the specific surface area and shielding of the capacitive effect originating from the N-containing functional groups. In addition, high concentrations of the KMnO<sub>4</sub> precursor caused the formation of MnO<sub>2</sub> with low crystallinity. The superior electrochemical performance of the MnO<sub>2</sub>/NBGC nanocomposite electrode was achieved from the synergistic impact of the hierarchical architecture according to appropriate MnO<sub>2</sub> loading on the porous carbon and the capacitive effect from the N-containing defects on the carbon material. These combined effects could

facilitate great adhesion of the MnO<sub>2</sub> nanoparticles on the substrate, limiting its large volume expansion and enabling fast ion and electron transport. The optimized carbon composite, namely 5-MnO<sub>2</sub>/NBGC, exhibited a high reversible capacity of about 760 mA h g<sup>-1</sup> at a current density of 186 mA g<sup>-1</sup> after 50 cycles, 488 mA g<sup>-1</sup> at 372 mA g<sup>-1</sup> and up to 390 mA g<sup>-1</sup> at 774 mA g<sup>-1</sup> after 150 cycles. It also showed good reversibility, with the coulombic efficiency reaching nearly 100%. Moreover, it delivered good rate capability with high specific capacity up to 388 and 301 mA h g<sup>-1</sup> even when tested under high current densities of 1860 and 3720 mA g<sup>-1</sup>, respectively, for at least 50 cycles. Compared to similar MnO<sub>2</sub>/carbon composite anode materials reported in previous studies, our proposed MnO<sub>2</sub>/NBGC anode material exhibits quite impressive performance and utilizes sustainable agricultural wasted, sugarcane bagasse as the base material. The approximated energy density calculation of the LFP-coupled 5-MnO<sub>2</sub>/NBGC full cell expectedly revealed a lower energy density compared to that of the LFP-graphite anode couple, regarding its higher nominal half-cell testing voltage. However, the good rate and cycling performance of the proposed 5-MnO<sub>2</sub>/NBGC anode may benefit potential usage in batteries for fast-rate applications with a longer lifetime. Here, the proposed MnO<sub>2</sub>/NBGC composites show potential for further development not only as promising electrode materials for rechargeable batteries (Li<sup>+</sup>, Na<sup>+</sup>, and K<sup>+</sup> batteries) and supercapacitors but also as active materials for other applications, such as catalysis and sensing.

## Author contributions

All authors contributed to the study conception and design. Material preparation, data collection and analysis were performed by Krittaporn Pongpanyanate, Supacharee Roddecha, and Chanita Piyanirund. The first draft of the manuscript was written by Krittaporn Pongpanyanate, and Supacharee Roddecha. All authors commented on previous versions of the manuscript. All authors read and approved the final manuscript.

## Conflicts of interest

There are no conflicts to declare.

## Acknowledgements

The authors would like to thank the Kasetsart University Research and Development Institute (KURDI) and Faculty of Engineering, Kasetsart University for the financial support during this project. We are also grateful for the equipment and academic facility by the department of Chemical Engineering, Kasetsart University. In addition, we would also like to thank Dirayanti for gathering final revised electrochemical performance assessment.

## Notes and references

- 1 K. Kim, G. Daniel, V. G. Kessler, G. A. Seisenbaeva and V. G. Pol, *Nanomaterials*, 2018, **8**, 608.





- 2 Y. Li, Y. Lu, P. Adelhelm, M. M. Titirici and Y. S. Hu, *Chem. Soc. Rev.*, 2019, **48**(17), 4655.
- 3 P. C. Rath, J. Patra, H. T. Huang, D. Bresser, T. Y. Wu and J. K. Chang, *ChemSusChem*, 2019, **12**(10), 2302.
- 4 K. Chayambuka, G. Mulder, D. L. Danilov and P. H. L. Notten, *Adv. Energy Mater.*, 2018, **8**(16), 1800079.
- 5 G. Wang, M. Yu and X. Feng, *Chem. Soc. Rev.*, 2021, **50**(4), 2388.
- 6 S. Lin, L. Mo, F. Wang and Z. Shao, *J. Alloys Compd.*, 2021, **873**, 159705.
- 7 L. Xie, C. Tang, Z. Bi, M. Song, Y. Fan, C. Yan, X. Li, F. Su, Q. Zhang and C. Chen, *Adv. Energy Mater.*, 2021, **11**(38), 2101650.
- 8 G. Zhong, H. Xie, Z. Xu, S. Xu, S. Xu, Z. Cai, X. Fu, W. Liao and R. Miao, *ChemistrySelect*, 2019, **4**(12), 3432.
- 9 K. Le Van and T. T. L. Thi, *Prog. Nat. Sci.: Mater. Int.*, 2014, **24**(3), 191.
- 10 S. Agarkar, P. Yadav, R. Fernandes, D. Kothari, A. Suryawanshi and S. Ogale, *Electrochim. Acta*, 2016, **212**, 535.
- 11 R. Luan, D. Xu, H. Pan, C. Zhu, D. Wang, X. Meng, Y. Li, M. Imtiaz, S. Zhu and J. Ma, *J. Energy Storage*, 2019, **22**, 60.
- 12 M. Chen, D. Yan, X. Zhang, Z. Yu, G. Zhu, Y. Zhao, S. Lu, G. Chen, H. Xu and A. Yu, *Mater. Lett.*, 2017, **196**, 276.
- 13 H. Wan and X. Hu, *Solid State Ionics*, 2019, **341**, 115030.
- 14 D. B. Babu and K. Ramesha, *Carbon*, 2019, **144**, 582.
- 15 P. Wu, M. Gao, S. Yu, M. Feng, S. Liu and J. Fu, *Electrochim. Acta*, 2020, **354**, 136681.
- 16 H. Xia, M. Lai and L. Lu, *J. Mater. Chem.*, 2010, **20**(33), 6896.
- 17 D. Yan, P. Yan, S. Cheng, J. Chen, R. Zhuo, J. Feng and G. Zhang, *Cryst. Growth Des.*, 2009, **9**(1), 218.
- 18 X. Jin, W. Zhou, S. Zhang and G. Z. Chen, *Small*, 2007, **3**(9), 1513.
- 19 H. T. Zhu, J. Luo, H. X. Yang, J. K. Liang, G. H. Rao, J. B. Li and Z. M. Du, *J. Phys. Chem. C*, 2008, **112**, 17089.
- 20 J. Ou, Y. Zhang, L. Chen, Q. Zhao, Y. Meng, Y. Guo and D. Xiao, *J. Mater. Chem. A*, 2015, **3**(12), 6534.
- 21 J. Jang, T. Kim, Y. Choi, I. Park, D. Lim, S. E. Shim and S. H. Baeck, *J. Nanosci. Nanotechnol.*, 2016, **16**(5), 5195.
- 22 X. Wang, X. Wang, W. Huang, P. J. Sebastian and S. Gamboa, *J. Power Sources*, 2005, **140**(1), 211.
- 23 T.-H. Ting, *J. Chin. Chem. Soc.*, 2009, **56**, 1225.
- 24 F. Gao, S. H. Qin, Y. H. Zang, J. F. Gu and J. Y. Qu, *N. Carbon Mater.*, 2020, **35**(2), 121.
- 25 Z. Fan, J. Yan, T. Wei, L. Zhi, G. Ning, T. Li and F. Wei, *Adv. Funct. Mater.*, 2011, **21**(12), 2366.
- 26 M. Jayashree, M. Parthibavarman, R. BoopathiRaja, S. Prabhu and R. Ramesh, *J. Mater. Sci.: Mater. Electron.*, 2020, **31**(9), 6910.
- 27 R. Muruganantham, F. M. Wang, R. A. Yuwono, M. Sabugaa and W. R. Liu, *Energy Fuels*, 2021, **35**(13), 10878.
- 28 A. P. Nowak, A. L. Oleksiak, B. Wicikowska and M. Gazda, *J. Solid State Electrochem.*, 2017, **21**(8), 2251.
- 29 L. Qie, W. M. Chen, Z. H. Wang, Q. G. Shao, X. Li, L. X. Yuan, X. L. Hu, W. X. Zhang and Y. H. Huang, *Adv. Mater.*, 2012, **24**(15), 2047.
- 30 J. Huang, Y. Lin, M. Ji, G. Cong, H. Liu, J. Yu, B. Yang, C. Li, C. Zhu and J. Xu, *Appl. Surf. Sci.*, 2020, **504**, 144398.
- 31 Z. Li, Z. Xu, X. Tan, H. Wang, C. M. B. Holt, T. Stephenson, B. C. Olsenab and D. Mitlin, *Energy Environ. Sci.*, 2013, **6**, 871.
- 32 W. Shi, Y. Zhang, Z. Q. Tian, Z. Pan, J. Key and P. K. Shen, *J. Power Sources*, 2018, **398**, 149.
- 33 J. G. Lee, Y. Kwon, J. Y. Ju, S. Choi, Y. Kang, W. R. Yu and D. W. Kim, *J. Appl. Electrochem.*, 2017, **47**(8), 865.
- 34 L. Xing, C. Cui, C. Ma and X. Xue, *Mater. Lett.*, 2011, **65**(14), 2104.
- 35 M. S. Wu, P. C. J. Chiang, J. T. Lee and J. C. Lin, *J. Phys. Chem. B*, 2005, **109**(49), 23279.
- 36 A. L. M. Reddy, M. M. Shaijumon, S. R. Gowda and P. M. Ajayan, *Nano Lett.*, 2009, **9**(3), 1002.
- 37 L. Feng, Z. Xuan, H. Zhao, Y. Ba, J. Guo, C. W. Su and X. Chen, *Nanoscale Res. Lett.*, 2014, **9**(1), 290.
- 38 H. Lindström, S. Södergren, A. Solbrand, H. Rensmo, J. Hjelm, A. Hagfeldt and S. E. Lindquist, *J. Phys. Chem. B*, 1997, **101**, 7717.
- 39 Q. Zhu, M. Wang, B. Nan, H. Shi, X. Zhang, Y. Deng, L. Wang, Q. Chen and Z. Lu, Core/shell nanostructured Na<sub>3</sub>V<sub>2</sub>(PO<sub>4</sub>)<sub>3</sub>/C/TiO<sub>2</sub> composite nanofibers as a stable anode for sodium-ion batteries, *J. Power Sources*, 2017, **362**, 147.
- 40 Y. H. Du, X. Y. Liu, X. Y. Wang, J. C. Sun, Q. Q. Lu, J. Z. Wang, A. Omar and D. Mikhailova, Freestanding strontium vanadate/carbon nanotube films for long-life aqueous zinc-ion batteries, *Rare Met.*, 2022, **41**(2), 415.
- 41 C. Liu, Q. Lu, M. V. Gorbunov, A. Omar, I. G. G. Martinez, P. Zhao, M. Hantusch, A. D. C. Permana, H. He, N. Gaponik and D. Mikhailova, Ultrasmall CoS nanoparticles embedded in heteroatom-doped carbon for sodium-ion batteries and mechanism explorations via synchrotron X-ray techniques, *J. Energy Chem.*, 2023, **79**, 373.
- 42 K. Zhong, X. Xia, B. Zhang, H. Li, Z. Wang and L. Chen, *J. Power Sources*, 2010, **195**(10), 3300.
- 43 K. Zhang, P. Han, L. Gu, L. Zhang, Z. Liu, Q. Kong, C. Zhang, S. Dong, Z. Zhang, J. Yao, H. Xu, G. Cui and L. Chen, *ACS Appl. Mater. Interfaces*, 2012, **4**(2), 658.
- 44 X. Zhang, Z. Xing, L. Wang, Y. Zhu, Q. Li, J. Liang, Y. Yu, T. Huang, K. Tang, Y. Qian and X. Shenc, *J. Mater. Chem.*, 2012, **22**(34), 17864.
- 45 H. Lai, J. Li, Z. Chen and Z. Huang, *ACS Appl. Mater. Interfaces*, 2012, **4**(5), 2325.
- 46 J. Deng, L. Chen, Y. Sun, M. Ma and L. Fu, *Carbon*, 2015, **92**, 177–184.
- 47 L. Li, A. R. O. Raji and J. M. Tour, *Adv. Mater.*, 2013, **25**(43), 6298.
- 48 A. Yu, H. W. Park, A. Davies, D. C. Higgins, Z. Chen and X. Xiao, *J. Phys. Chem. Lett.*, 2011, **2**, 1855.
- 49 Y. Son, H. Cha, C. Jo, A. S. Groombridge, T. Lee, A. Boies, J. Cho and M. De Volder, *Mater. Today Energy*, 2021, **21**, 100838.

